Tunable organic solvent nanofiltration in self-assembled membranes at the sub-1 nm scale

Yizhou Zhang[1,2], Dahin Kim[2], Ruiqi Dong[2], Xunda Feng[3], Chinedum O. Osuji[2*]

[1]Key Laboratory of Organic Compound Pollution Control Engineering, Ministry of Education, and School of Environmental and Chemical Engineering, Shanghai University, Shanghai 200444, China.

[2]Department of Chemical and Biomolecular Engineering, University of Pennsylvania, Philadelphia, PA 19104, United States.

[3]Center for Advanced Low-dimension Materials, State Key Laboratory for Modification of Chemical Fibers and Polymer Materials, Donghua University, Shanghai 201620, China.

[*] Corresponding author. Email: cosuji@seas.upenn.edu

ABSTRACT

Organic solvent-stable membranes that exhibit strong solute selectivity and high solvent permeance have the potential to transform the energy footprints of chemical separation processes. A key but elusive goal is the development of materials with uniform, well-defined pores at the 1 nm scale, the sizes of which can be tuned in small increments with high fidelity. Here, we investigate the fabrication and transport properties of a class of organic solvent-stable nanoprous membranes derived from self-assembled liquid crystal mesophases. Membranes are realized by coating a *ca*. 200 nm thick film of the mesophase onto mechanical support membranes using a solution process, followed by internal cross-linking of the hexagonally arrayed cylinders formed by the self-assembly of the constituent surfactant mesogen. The transport regulating dimensions are defined by the geometry of the mesophase and can be controlled in fine increments of ~0.1 nm by modifying the structure of the mesogen, or the composition of the lyotropic mesophase. The highly ordered nanostructure affords new opportunities for the systematic design of organic solvent nanofiltration membranes with tailored selectivity and permeability, and for understanding and modeling rejection in nanoscale flows. As such these membranes represent progress towards the goal of enabling precise organic solvent nanofiltration.

ONE-SENTENCE SUMMARY

Self-assembled membranes with uniform pores precisely tunable in 0.1 nm steps have been developed for organic solvent nanofiltration.

INTRODUCTION

Separation processes in the chemical industry account for approximately 15% of total global energy consumption (*1*). This high rate of consumption is due to the prevalence of thermal processes in which phase changes are an intrinsic part of the separation, *cf.* distillation, evaporation, and drying (*2*). Organic-solvent nanofiltration (OSN) is an emerging molecular separation technology that features an order of magnitude lower energy spend, and is recognized for its potential to significantly alter the landscape in the chemical industry in terms of energy efficiency of separation processes (*3-5*). Progress in recent years has delivered working OSN based on solvent-compatible polymers, using conventional materials, typically processed through phase inversion, interfacial polymerization, or direct coating of thin-film composite (*4, 6, 7*). In these cases, separation occurs primarily due to permselective transport in dense selective layers, as opposed to separation by sieving during flow through nanopores. While high permeability membranes are desired for maximizing process throughput, there exists an intrinsic trade-off between solvent permeability and solute selectivity in OSN (and other) membranes (*8, 9*). For conventional OSN membranes operating by permeselective transport, this trade-off arises due to the presence of heterogeneous and non-uniform permeation pathways (*10*). The large-scale use of these membranes is often not viable due to their low solvent permeance, *e.g.,* ~1 L m^{-2} h^{-1} bar^{-1} for methanol (*4*). Additionally, and importantly, selectivity is challenged by the diminished role of electrostatics in the low polarity environment of organic solvents compared to aqueous media – the selectivity of aqueous nanofiltration membranes often has a strong contribution from electrostatic interactions between traveling solutes and the membrane (*11, 12*). In the absence of such a contribution in OSN membranes, effective solute rejection is more heavily reliant on the physical characteristics of the transport regulating features in the system, *viz.* the pore size and the size distribution in nanoporous membranes, or the size of free-volume elements and their distribution, in dense membranes.

Recent studies have highlighted the potential of polymeric materials for effective OSN in several contexts. Livingston and co-workers proposed a sophisticated yet practical methodology to prepare crumpled, sub-10 nm thickness free-standing polyamide films with high permeance that were incorporated as selective layers in a composite membrane (*13*). Alternatively, contorted 1-D

ladder-like polymers with intrinsic microporosity (PIMs) leverage inefficient chain packing to create inter-connected sub-2 nm volumes, and have demonstrated solvent permeance two orders of magnitude higher than Starmem240 commercial membranes (*14*). The rapid structural relaxation of 1-D PIMs presents a hindrance to their implementation in ultra-thin films. 3-D PIMs are more robust in this regard, and a designed 3-D polyarylate system with enhanced microporosity achieved a high methanol permeance of ~8 L m^{-2} h^{-1} bar^{-1} based on a 20 nm thick membrane (*15*). Work by Liang *et. al* used surface-initiated polymerization of dibromobenzene to generate rigid pores with well-defined structural persistence that efficiently separate ~1.5 nm size solutes with methanol permeances of ~20 L m^{-2} h^{-1} bar^{-1} (*16*). The preparation of high permeance (> 10 L m^{-2} h^{-1} bar^{-1}) OSN membranes with sub-1 nm selectivity remains elusive however. Such membranes are highly desired for the separation of low molar mass solutes (< 300 Da), and for solvent purifications. Covalent organic and metal-organic frameworks (COFs, MOFs) offer promise in this regard in their ability to present tailored pores at sub-1 nm length scales (*17-19*). However, the straightforward fabrication of defect-free sheets of such materials over macroscopic areas presents a critical challenge.

Self-assembled lyotropic mesophases based on small molecules (molar mass ~500 Da) are characterized by thermodynamically prescribed morphologies with well-defined structural periodicities (*20-22*). Appropriately prepared, these materials can provide transport regulating features at ~1 nm length scales associated with the lamellar, cylindrical, or gyroid motifs (*23-25*), and their potential in membrane applications is highlighted in prior research (*26-29*). The ordered nanostructure circumvents the challenges associated with the dispersity of transport regulating features in conventional membranes highlighted earlier, and offers the compelling possibility of overcoming the selectivity-permeability trade-off seen in current OSN membranes. To first order, the transport regulating feature size of a self-assembled mesophase is determined by the size of the constituent molecular species, and its concentration in the lyotropic system. The utilization of self-assembled systems for OSN therefore offers the attractive possibility of fine-tuning the cutoff-characteristics of membranes by appropriately altering the size of the molecular building blocks, and/or their concentration in the phase. For example, work by Gin and co-workers polymerized bicontinuous cubic (Q_I) mesophases from various surfactant molecules to ensemble membranes with pore sizes between 0.75 and 0.96 nm (*30, 31*).

While self-assembled materials hold significant potential for improved OSN performance, we are not aware of any work to date implementing self-assembled nanostructures for OSN in the 1 nm regime. This is likely due to the significant challenges associated with doing so – apart from the difficulty associated with maintaining membrane stability in organic solvents with different polarities, the difficulty of preserving self-assembled nanostructures in thin-films (*32-34*), and the potential need for nanostructural alignment to ensure good permeance (*35-37*) represent significant obstacles in the fabrication of practical OSN membranes with ordered nanostructure. A recently developed strategy addresses these challenges however. The internally cross-linked cylinders from a direct lyotropic hexagonal (H_I) mesophase present an attractive medium for nanofiltration, due to the bicontinuous nature of the solvent transport, and the well-defined ~1 nm slit-like pores provided by the space between the surfaces of nearest-neighbor cylinders uniformly oriented in the plane of the film (*38, 39*).

Here, we introduce a method for the fabrication of cross-linked hexagonal mesophase-based membranes for OSN and present data on their solute rejection and permeability characteristics. We explore a series of mesophases prepared using different alkyl chain length surfactants and cross-linking chemistries with H_I domain spacing tailored from 3.1 to 3.9 nm. The resulting membranes exhibit systematic variation in pore size that is manifested accordingly in their transport characteristics. In comparison to several recently reported polymeric OSN membranes, the mesophase-derived membranes reported here are highly ordered, and display higher solvent permeabilities. These nanostructured membranes operate effectively in sieving-based separation, as demonstrated by solute rejection experiments in different organic solvents. The self-assembled materials explored here may provide a new paradigm for membranes with precisely tunable nanostructure for demanding OSN applications.

RESULTS AND DISCUSSION

We employed a series of polymerizable surfactants that feature a hydrophobic ethyl acrylate group and alkyl tail jointly linked to a hydrophilic quaternary ammonium head group. These molecules were synthesized using a one-step Menshutkin reaction targeting different carbon

chain lengths (*38*). Mesophases are prepared by mixing the surfactants with glycerol (containing 10 wt.% water) and a selected cross-linker (either pentaerythritol tetraacrylate (PETA, t) or hexanediol diacrylate (HDDA, d)) with designated weight fractions, shown in Fig. 1. 4 polymerizable surfactants were used with differing alkyl chain lengths corresponding to 18 (n8), 16 (n7), 14 (n6) and 12 (n5) methylene groups in the hydrophobic tail, where the n stands for repeating ethyl unit, as shown in Fig. 1A. Each surfactant was screened to identify appropriate compositions that provided stable hexagonal lyotropic mesophases at room temperature. All 4 species formed H_I mesophases with unit cell dimensions ranging from ~3-4 nm. Here we designate the mesophases according to the type of surfactant molecule and the cross-linker presented within, as n5t, n6t, n6d, n7d, and n8d, respectively. Fig. 1B provides the schematic of the proposed OSN membranes and the associated transport regulating dimensions templated by lyotropic mesophases.

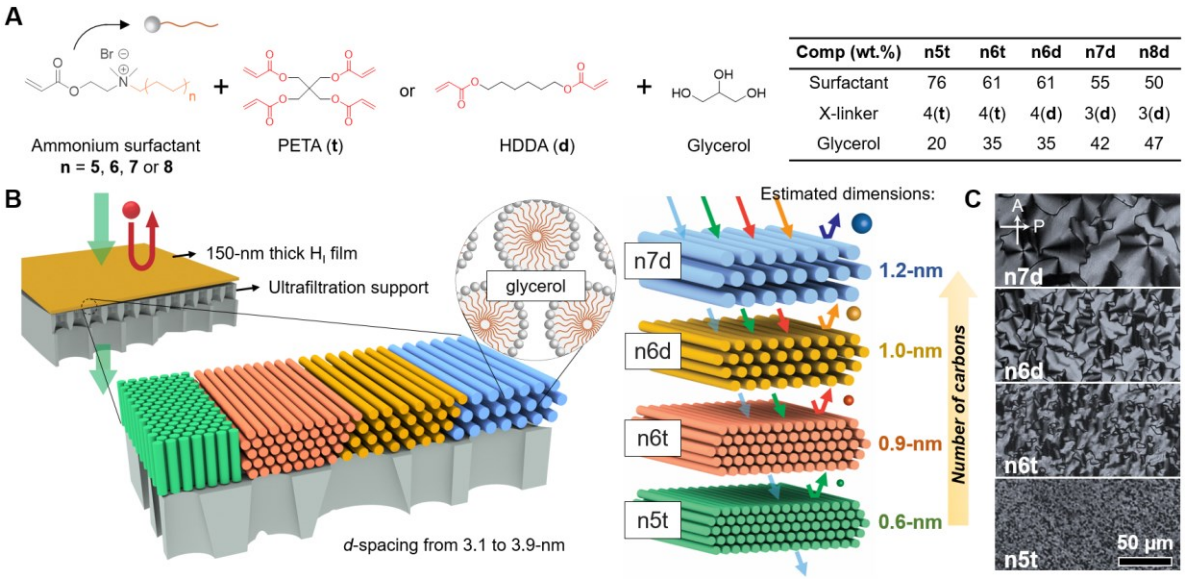

Comp (wt.%)	n5t	n6t	n6d	n7d	n8d
Surfactant	76	61	61	55	50
X-linker	4(**t**)	4(**t**)	4(**d**)	3(**d**)	3(**d**)
Glycerol	20	35	35	42	47

Fig. 1. Schematic illustration of self-assembled OSN membranes with pore sizes tuned by tailoring the lyotropic mesophase chemistry. (**A**) Chemical structure of the polymerizable surfactants and other components (PETA or HDDA cross-linkers; glycerol containing 10% water) of the mesophase. The specific mesophase compositions are tabulated. The alkyl chain length is varied by changing n (n= 5, 6, 7, and 8) to target nanostructured membranes with different pore sizes. (**B**) Illustration of different H_I thin-films with unit cell dimensions d_{100} ranging from 3.1 to 3.9 nm prepared atop ultrafiltration supports. The cylinders of the mesophase may orient vertically (cf. green cylinders) or horizontally. For parallel cylinders, the transport regulating dimension is the distance between neighboring cylinder surfaces, and this ranges from ~0.6 -1.2 nm for the 4 systems studied in detail. (**C**) Magnified POM micrographs of the polymerized H_I thin-films reveal the preservation of their original textures from the lyotropic mesophase.

Glycerol is a low volatility liquid (vapor pressure < 1 torr at 20 °C). It is used as the medium for lyotropic assembly to facilitate structure retention during solution-based processing by avoiding changes in composition due to evaporative loss. The components of the mesophase were dissolved in ethyl acetate at 10 wt% (vapor pressure ~70 torr at 20 °C) to yield a low viscosity solution. The solution was spin-coated on various substrates, followed by ultraviolet (UV)-initiated cross-linking in a nitrogen atmosphere to produce solid films. The mesophase structure in fabricated thin films was examined by polarized optical microscopy (POM) coupled with grazing-incidence small-angle X-ray scattering (GISAXS) on different substrates. Comparison of the optical textures of the mesophase in its initial lyotropic gel state, versus those in the cross-linked gel reveals excellent retention of the hexagonal structure after UV-induced cross-linking (see fig. S1). Magnified POM images of the polymerized mesophases are shown in Fig. 1C.

GISAXS was conducted for thin films prepared by spin-coating 10 wt.% mesophase solutions onto polished silicon wafers, and on wafers coated with a thin layer (~3 um) of polyvinyl pyrrolidone (PVP). PVP surfaces were used as its orthogonal solubility relative to the cross-linked mesophase makes it a good candidate for a sacrificial layer for membrane fabrication on porous supports (discussed below). Data are shown in Figs. 2A, B. For mesophases containing surfactants with hydrophobic tails shorter than 18 carbons, the Bragg reflections from 1D GISAXS data (generated by azimuthal integration of the 2D data) from the PVP-H_I composites occur at scattering vector ratios of 1: $\sqrt{3}$: $\sqrt{4}$. This is consistent with high-fidelity retention of the H_I mesophase structure after cross-linking (Fig. 2B). However, the cross-linking of the n8d mesophase was accompanied by disruption of the mesophase order, as manifested by a marked change in optical textures observed by POM (fig. S2). GISAXS data (fig. S3) indicate that the n8d system undergoes a transformation to a lamellar structure during cross-linking, and so this system was not extensively studied.

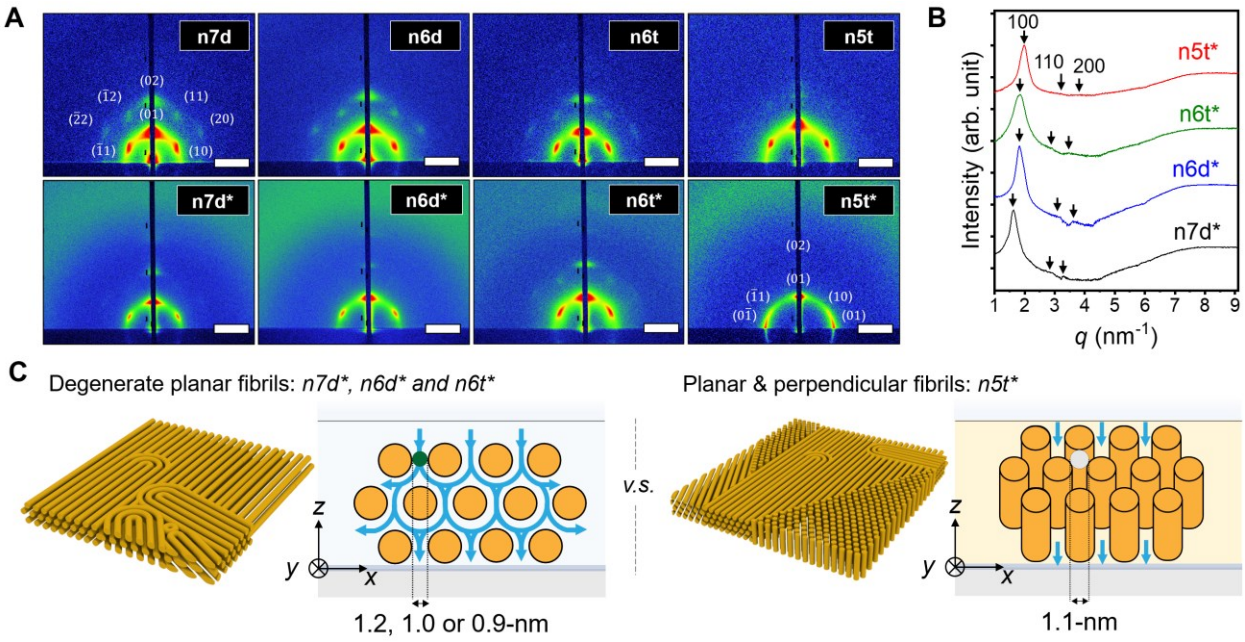

Fig. 2. Structural characterization and dimensional analysis of different H_I thin-films cast from 10 wt.% mesophase solutions. (**A**) 2D-GISAXS data from samples prepared by spin-coating and cross-linking different mesophase thin-films atop either bare silicon wafers (top row) or on polyvinyl pyrrolidone (PVP, bottom row, noted with *). The GISAXS data reflect the existence of hexagonal mesophases with different orientations of the cylindrical nanostructures. The scale bar is 2 nm^{-1}. (**B**) 1D GISAXS data acquired from H_I coating on PVP-covered surfaces. (**C**) Schematic showing the estimated critical dimensions for transport within the mesophases as inferred from the X-ray data for n7d*, n6d*, n6t* and n5t* systems. The calculations are based on the assumption that the bromide anions dissociate from the surfactant molecule.

The 2D GISAXS data provide important information regarding the orientation of the nanostructures produced by spin-coating and cross-linking the mesophases. The hexagonal symmetry observed for n7d, n6d, and n6t on both silicon and PVP surfaces indicates that the cross-linked cylinders in the system are oriented with their long axes parallel to the plane of the substrate. By contrast, for n5t, while such a planar configuration was observed on silicon substrates, a mixture of planar and perpendicular, or vertical, cylinders was observed for films prepared on PVP. The existence of vertically oriented cylinders is implied by the concentration of scattering intensity along the equatorial line of the scattering plane. The observed mixture of planar and perpendicular cylinders was found for n5t samples prepared from a broad range of surfactant concentrations (fig. S4). We surmise that the effect of the PVP on the morphology is more pronounced for this 12-carbon alkyl surfactant system, relative to the others. One possibility is that the planar

configuration is metastable, and kinetically dictated during the rapid assembly during spin-coating, following which the low mobility of longer-chain surfactant mesophases precluded rearrangement (*40, 41*). We consider it more likely however that the observed differences are related to differences in the energetics of the substrate interactions, which can vary considerably with composition and molar mass of the constituent species. For the planar arrangements, the orientation of the cylinders in the plane of the film is not constrained, as evidenced by the lower intensity of the off-meridional (10) reflections relative to the meridional (01) reflection. Further, the discrete azimuthal intensity variation indicates that there is a preferred orientation of the hexagonal lattice in the films, with the close-packed planes parallel to the film surface.

The display of planar vs. perpendicular orientations of the cylinders has important implications for selective transport in the fabricated films. The transport limiting dimension for solutes traveling through the film along its thickness (the z-axis) is larger for perpendicular cylinders than it is for planar cylinders (fig. S5). The ratio between the two is the diameter of the circular void at the center of a triangle connecting the centers of 3 nearest neighbor cylinders relative to the distance between surfaces of any pair of nearest neighbor cylinders. This ratio, $P = 2\delta/S_x = (4/3 - \xi)/[(4/3)^{1/2} - \xi]$ where $\xi = (8\varphi/\sqrt{3}\pi)^{1/2}$ for a system with volume fraction of cross-linked cylinders given by φ. For example, with $\varphi = 0.50$, P is 1.6. From the d_{100} spacings provided by GISAXS, we calculate the transport limiting dimensions associated with the planar and mixed planar/perpendicular orientations of the cylinders. For n5t, the transport limiting dimension is 2δ, associated with travel parallel to the cylinder axes, whereas for the other mesophases, it is the smaller critical dimension, S_x, associated with travel orthogonal to the cylinders. The transport limiting dimensions ranged from ~0.9 to 1.2 nm, as shown in Fig. 2C (additional details in fig. S5). Additionally, this dimension is readily tunable by adjusting the surfactant weight fractions in the lyotropic phase (additional mesophase with structural analysis shown in figs. S6 and S7), and was tailored in fine increments of ~0.1 nm (fig. S8). The interplay of composition with molecular structure provides a rich design space for creating fit-for-purpose membranes with tailored dimensions.

Thin (i.e. less than ~200 nm) membranes were prepared for the characterization of transport properties by spin-casting thin layers of the lyotropic mesophases on sacrificial layer coated ultrafiltration supports. The sacrificial layer prevents the infiltration of the mesophase solution into

the support membrane during casting. The fabrication process is illustrated in Fig. 3. A PVP film of ~3 µm thickness was coated on polyvinylidene fluoride (PVDF) ultrafiltration membranes by spin coating. Subsequently, mesophase solutions in ethyl acetate were directly spin-coated on the composite; PVP is insoluble in ethyl acetate, and is therefore preventing entry of the mesophase into the PVDF support. The mesophase thin-film was kept quiescently under ambient conditions for ~1 minute to facilitate solvent evaporation, following which it was photopolymerized by exposure to UV light. The resulting composite membranes were permeated with DI water in a stirred dead-end filtration cell for ~12 hours, until steady permeances were recorded, indicating that the sacrificial layer had been fully removed. Membranes were kept in the filtration cell for the weeks-long duration of their testing and were thereafter removed for imaging by SEM. Images are shown in Fig. 3B. Micrographs of high magnification views with false color overlays delineating the selective layers are shown in fig. S9. Additionally, no delamination of the selective layer from the underlying support was observed during this period.

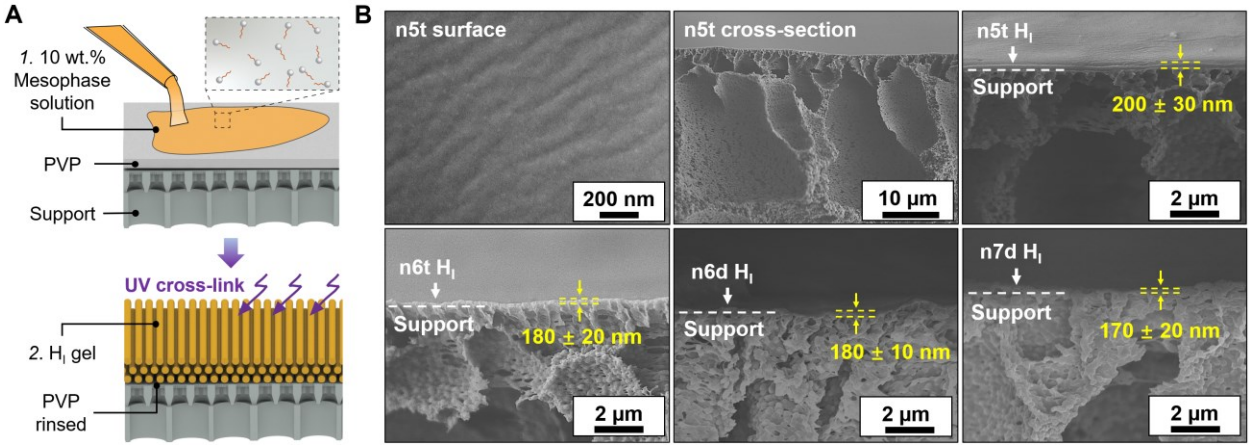

Fig. 3. Schematic illustration of the fabrication of thin mesophase-derived membranes and images of their resulting structure. (**A**) Schematic describing the self-assembled H_I thin-film composite membrane fabrication process. (**B**) Top-view scanning electron microscopy (SEM) images of a cross-linked n5t H_I mesophase after thoroughly rinsing to remove the PVP sacrificial layer, and cross-sectional views of n5t, n6t, n6d, and n7d membranes atop PVDF supports after removal of PVP sacrificial layers. Error bars correspond to 95% confidence interval from a minimum of 3 measurements.

The transport properties of the membranes were first characterized using aqueous solutions (dielectric constant, ε = 80.2) containing ~1.2 nm hydrodynamic diameter polyethylene glycol (600 g mol^{-1} PEG) (*42-44*). The PEG possesses no significant or persistent shape anisotropy. Hence, the rejection data with PEG provides a realistic representation of the minimum dimension of the slit-like pores in between cylinders. This situation contrasts with that of highly anisotropic solutes that could in principle transit through the slit-like pores despite having a molar mass above the nominal cut-off (*39*). The measured hydraulic permeance is in good agreement with theoretical estimates made for ordered planar oriented cylinders (*45*), and a hypothetical mixture of perpendicular and planar orientations (*46*), as shown in fig. S10. The observed rejections were corrected for the effects of concentration polarization (~0.3 to 3 % change) using the correlation developed by Zeman and Zydney (*47*). Complete rejection was observed for membranes based on mesophases with calculated limiting dimensions lower than 1.2 nm (assuming complete ammonium bromide dissociation), as shown in Fig. 4A. The n7d membranes, with a transport regulating dimension estimated at 1.2 nm, demonstrated a rejection of 83%. The transport regulating dimension is estimated on the simplifying assumption that the Br^- counterion is a fixed part of the mobile phase. It is likely that the degree to which Br^- is part of the stationary *vs*. the mobile phase is a strong function of solvent polarity, and we anticipate that the effective pore size may be modestly larger in high polarity media such as water that favors dissociation of the counterion from the quaternary ammonium co-ion. Nevertheless, the observed rejections, under convective transport conditions, are unambiguous regarding the regime of solute sizes that can be effectively filtered by the membranes.

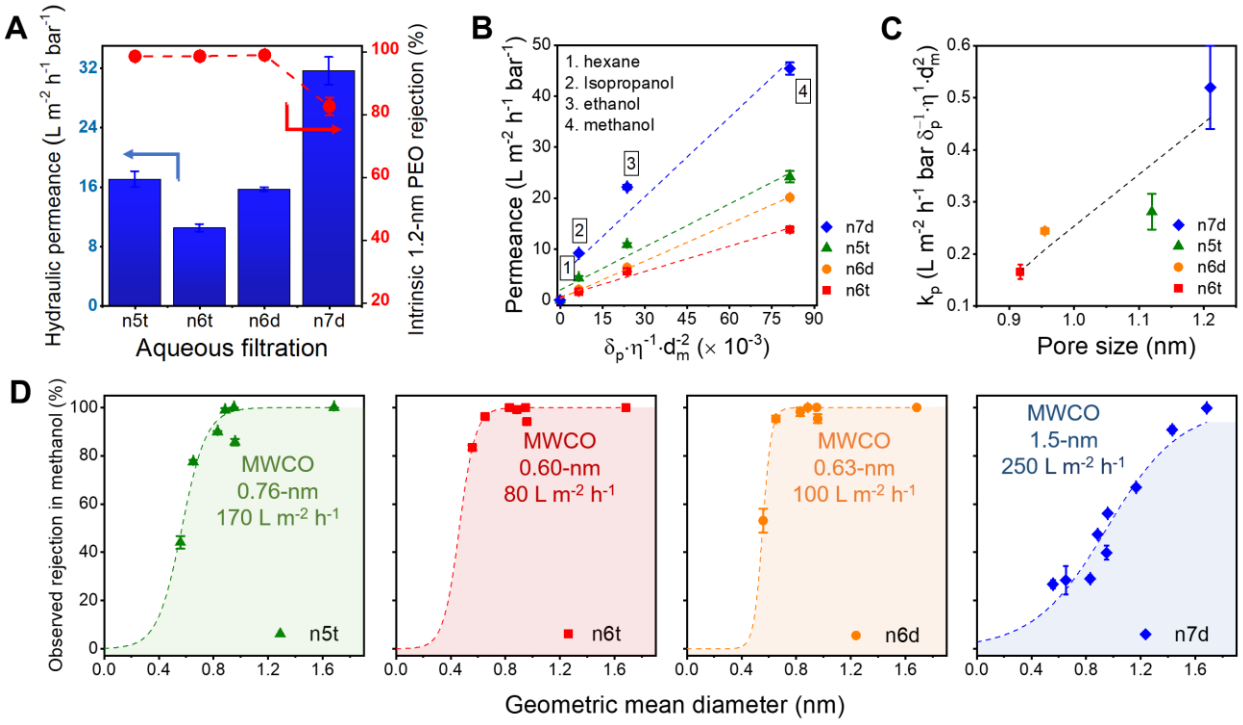

Fig. 4. Nanofiltration performance of the H_I templated membranes in aqueous and organic environments. (**A**) A survey of transport performance among four H_I membranes in DI water. The single solute rejections of 600 g mol^{-1} polyethylene glycol (PEG) molecule are displayed with the hydraulic permeance. (**B**) Pure solvent permeances follow a phenomenological model composed of solubility parameter, viscosity, and solvent molar diameter. The dashed lines represent the linear regressions that derive the proportionality constant *A* proportional to the calculated membrane pore sizes shown in (**C**). (**D**) Observed solute rejection performance measured by permeating different dye molecules dissolved in methanol across the membrane at a consistent transmembrane pressure 5 bar. The observed molecular weight cut-offs (MWCOs) are located at 0.6, 0.63, 0.76, and 1.5 nm for n6t, n6d, n5t, and n7d membranes. The curves are fitted with a sigmoidal model. Error bars correspond to 95% confidence interval from a minimum of 3 replicates. Where absent, the error bars are smaller than the symbol size. The methanol flux recorded during the neutral red rejection is listed with the MWCO curves.

Prior to performing organic solvent filtration experiments, we examined the stability of the membranes on exposure to various solvents by GISAXS measurements using n6d as a model system. Cross-linked films on silicon wafers were immersed in various solvents, and then vacuum dried for subsequent structural characterization. GISAXS data show a preservation of structure, as manifested by retention of hexagonally arranged Bragg spots with a d_{100} spacing of ~3.4 nm as detailed in fig. S11. These data indicate that the membranes retain their nanostructure in the

presence of the organic solvents considered here. It is worth noting that the choice of solvents was constrained not by the stability of the cross-linked mesophase, but by that of the support membrane.

Organic solvent permeation experiments were conducted in dead-end filtration cells at ~20 °C. Data are shown in Fig. 4B. Permeance was derived from the linear regression of solvent flux to the applied pressure detailed in fig. S12. The solvent permeances and solute rejections did not change measurably over the weeks-long durations of the permeation tests. This steady transport performance indicates that the nanostructures within the membrane, and the composition overall, are highly stable under the test conditions used here. The highest permeance recorded was 45 L m^{-2} h^{-1} bar^{-1} for passage of methanol through a n7d membrane. The same membrane showed a ~5× reduction in permeance for isopropanol, while hexane exhibited no measurable permeation, even at a high transmembrane pressure of 28 bar.

While the standard continuum models for transport in nanoporous membranes invoke viscosity as the only fluid property that impacts permeance, for nanofiltration membranes, and specifically for OSN, permeance is affected by factors beyond viscosity. A phenomenological model invoking the diameter of the solvent molecule, the solubility parameter and the dynamic viscosity was developed by Buekenhoudt *et al*., to account for permeance of various solvents in porous NF and UF ceramic membranes (*48*), and applied by Livingston and co-workers successfully for polyamide thin films (*13*). The model implicitly seeks to account for solvent-membrane interactions, and the effects of excluded volume on solvent species transport, and momentum diffusion, though there are several caveats given the correlation among the three representative parameters. As advanced by Livingston and co-workers, based on correlations highlighted by Buekenhoudt *et al*., the model provides a transport parameter, k_p and posits that permeance scales linearly with the solvent parameter $\delta_p \eta^{-1} d_m^{-2}$, *i.e.* that permeance P is proportional to k_p as

$$P = k_p \left(\frac{\delta_p}{\eta^1 d_m^2} \right) \quad (1)$$

where δ_p is the polarity factor of the solubility parameter, η is the solvent viscosity and d_m is the solvent molecular diameter. Our solvent permeation results are well-described by the model as shown by the data for 4 different solvents, in each of the 4 membranes (Fig. 4B). Further, the

constant of proportionality, k_p shows a linear relationship with pore size (Fig. 4C). The significance of this pore size dependence is unclear. Buekenhoudt *et al*. considered water flux normalized data and remarked that pore size may play an indirect role in the water permeance normalized proportionality factor, C, contained therein, and defined as $(P\eta)/(P_w\eta_w) - 1 \propto C\,(\delta_{tot}/\delta_{tot,w} - 1)$, with this factor decreasing exponentially for larger pores. However, the proportionality depended also on the surface chemistry of the commercially produced Inopor membranes, which varied even for membranes with the same nominal pore size, and so the dependence of the proportionality factor to pore size could not be unambiguously delineated. Further, the pore sizes of the membranes were broadly distributed, which could smear out a clear role regarding pore size. Here, our membranes provide precise, small changes in transport regulating dimensions that are narrowly distributed. Our analysis of water flux normalized data excluding the hexane permeance (fig. S13) suggests that the Buekenhoudt proportionality factor C scales linearly with pore size for our membranes. We anticipate that these membranes may prove useful in generating data against which existing concepts for nanoscale transport may be evaluated, or using which new concepts may be developed.

Rejection experiments were performed in methanol (ε = 32.7) using a constant transmembrane pressure 5 bar, and a variety of molecular solutes with sizes in the range of 0.5-2 nm, at a concentration of 50 μM, while the permeate was collected after the steady-state was achieved. The membranes displayed distinct rejection characteristics. As shown in Fig. 4D, the molecular weight cut-off (MWCO) varied from ~0.6 to 1.5 nm across the 4 types of membranes considered. This range of sizes corresponds to ~290 to 800 g mol^{-1} in terms of molar mass (space-filling models for each solute are displayed in fig. S14). The methanol flux recorded during the nanofiltration of neutral red (NR, 289 g mol^{-1}) are indicated on each MWCO curve. Membranes n6d and n6t demonstrate similar selectivity with only a minor difference in their MWCOs. (320 vs 290 g mol^{-1} respectively). This is unsurprising given the single Angstrom difference in their lattice constants, with d_{100} spacings of 3.4 and 3.5 nm. Meanwhile, the n8d membrane with the largest d-spacing of 3.9 nm exhibited a cut-off at 1.5 nm, and correspondingly displayed the highest solvent flux, 250 L m^{-2} h^{-1} in neutral red solution. For n5t membranes, the large MWCO of 350 g mol^{-1} reflects the larger transport limiting dimension in this system despite having the smallest d-spacing of 3.1 nm. As discussed earlier, this is due to the presence of some vertically oriented cylinders, which result in larger pores being available for transport than the case for all planar cylinders.

Fig. 5A provides a summary of methanol permeance versus the reciprocal membrane thickness for our mesophase-derived membranes, along with data for several recently reported polymeric OSN membranes. The current work validates the concept of uniformly nanostructured organic solvent nanofiltration membranes, and demonstrates the tunability inherent in the mesophase self-assembly. Nonetheless, these membranes exhibit higher permeance, and in the majority of cases, also higher permeability, relative to recently reported systems. A more detailed performance comparison is provided by considering solute rejection as a function of solvent (methanol) permeance, shown in Fig. 5B. The data highlight the improved solvent permeance and the superior permeability (fig. S15) at high rejection levels. Note that in the case of n7d the data are uncorrected for the effects of concentration polarization, which negatively affect rejection under high flux conditions. We examined solute rejection performance in isopropyl alcohol (IPA, $\varepsilon = 19.9$) at a consistent solvent flux ~10 L m^{-2} h^{-1}. As shown in Fig. 5C, the n7d membrane exhibits a higher rejection to both acid fuchsin (AF) and methyl orange (MO) in the IPA rejection experiment than in methanol, and demonstrates an improved MWCO of ~0.9 nm (590 g mol^{-1}). Associated UV-Vis spectra and images are shown in the fig. S16. The reduction in MWCO in IPA *vs*. methanol is likely a result of concentration polarization under the higher flux conditions during methanol operation. Enhanced ion-pairing in IPA relative to methanol due to dielectric permittivity differences may also contribute to this effect.

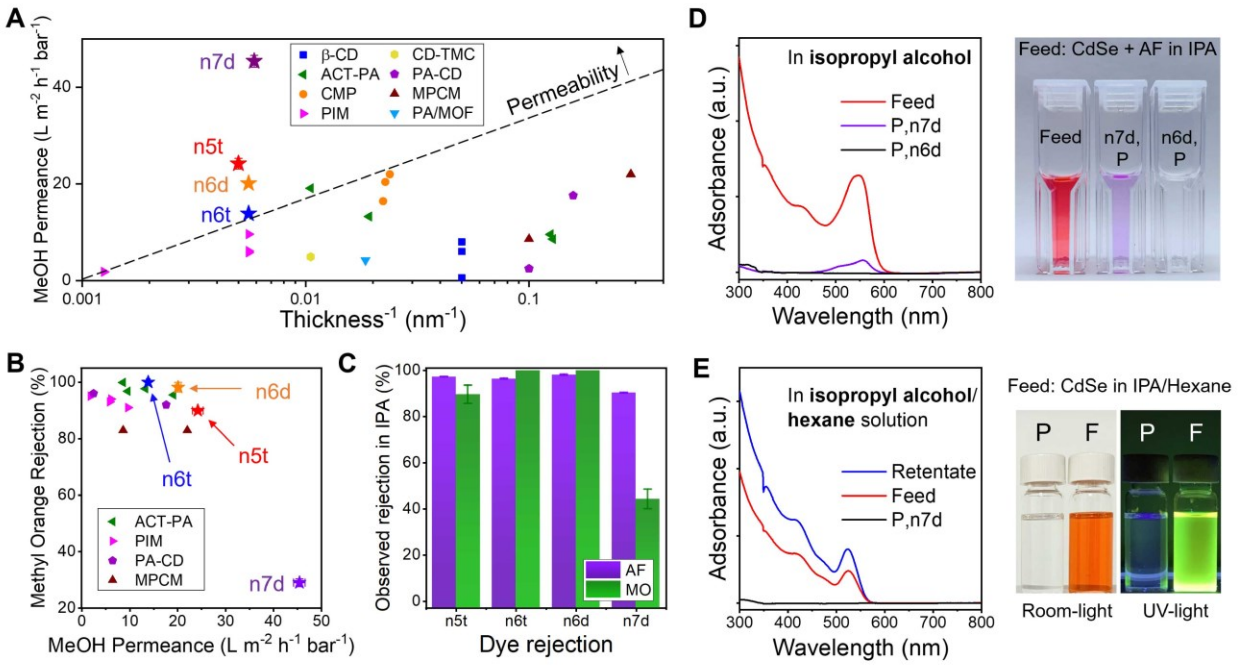

Fig. 5. Single solute and dual, or competitive, organic solvent nanofiltration performance. (**A**) Methanol permeance as a function of membrane thickness for H_I membranes compared to other reported polymeric OSN membranes including polyamides (ACT-PA, PA/MOF) (*13, 49*), PIMs (*14, 15*), rigid conjugated microporous polymers (CMP) (*16*), beta cyclodextrin-terephthaloyl chloride (β-CD) (*50*), cyclodextrin-trimesoyl chloride (CD-TMC) (*51*), polyamide-cyclodextrin (PA-CD) (*52*), and molecularly porous polyamide (MPCM) (*53*). (**B**) Comparison of the methyl orange rejection and methanol permeance for the H_I membranes to other materials in literature. (**C**) Single solute rejection data of different mesophase templated membranes for acid fuchsin (AF) and methyl orange (MO) dissolved in isopropyl alcohol. (**D**) UV-visible spectrum and photograph for competitive separation of CdSe nanoparticle and AF dissolved in isopropyl alcohol, by n6d and n7d membranes. (**E**) UV-Vis data and photographs of the luminescent quantum dots demonstrating the n7d solute rejection in a solvent mixture of 5 to 5 (by volume) isopropyl alcohol to hexane solution. Error bars are propagated 95% confidence limits derived from multiple measurements. Where absent, the error bars are smaller than the symbol size.

The filtration of particulate species, and competitive filtration of particulate and molecular species were investigated using 2.7 nm diameter CdSe quantum dots (electron microscopy images in fig. S17), and mixtures of these dots with molecular dyes, respectively. Filtration of CdSe suspended in IPA using n6d and n7d membranes showed complete rejection of CdSe (fig. S18) as expected given the < 1 nm MWCO based on rejection data for these membranes when confronted with molecular dyes in IPA (Fig. 5C). Data for competitive rejection experiments with CdSe in the presence of AF in IPA are shown in Fig. 5D. Both membranes rejected CdSe completely. The

n6d membrane rejected AF completely, but for n7d, the rejection was 90 %. In a second experiment using a smaller dye, MB, CdSe was again completely rejected, whereas the rejection of MB was 85% and 60% for n6d and n7d, respectively (fig. S19). These results highlight the efficacy of these membranes for selective solute separations.

We also examined the filtration of CdSe quantum dots dispersed in a 1:1 vol. mixture of IPA and hexane, using n7d membranes. Results are shown in Fig. 5E. The quantum dots were completely rejected as expected. Additionally however, analysis of the permeate showed evidence of differential transport of IPA and hexane through the membrane. CdSe photoluminescence (PL) is sensitive to the nature of the surrounding solvent, and in particular, PL is reduced in polar solvents such as IPA, relative to hexane (*54*). Results show enhanced PL in the retentate (fig. S20) relative to the original feed, indicating that HEX enrichment occurred in the feed, and IPA enrichment in the permeate. Differential transport is expected on the basis of the differences in solubility parameters of the solvents, as well as molecular size. The extent of the enrichment could not be quantitatively determined from the PL data however. While these results are preliminary, they are consistent with the expectation that differential solvent transport will occur in these systems, and highlight potential utility for these membranes in solvent separations.

CONCLUSION

Our work demonstrates a strategy to prepare self-assembled membranes for high-performance OSN in the 1 nm regime. Fabrication of thin mesophase-derived membranes was enabled by a facile solution process with the resulting cross-linked materials exhibiting stability in a range of organic solvents, and the membranes demonstrated stable filtration performance. Variation of the size (alkyl chain length) of the self-assembling constituent species provides a reliable handle for tuning the transport limiting dimensions of the derived membranes, with MWCO points observed ranging from 0.6 to 1.5 nm. Solvent transport is well-described by a phenomenological model invoking viscosity, solubility parameter, and solvent molecular size. Differential solvent transport was demonstrated, highlighting the potential for solvent separations. These membranes stand out for their high permeabilities relative to a broad range of amorphous

polymeric membranes. We anticipate that the approach demonstrated here can be extended to other mesogens, perhaps tailored for OSN or other separations of interest. Further, we expect that the current solution-based spin-coating method can be migrated to roll-to-roll solution processing using blade or dip-coating for the membrane fabrication at a larger scale. This work may facilitate the development of new energy-efficient membrane applications, especially for organic solvent applications that request exquisite sieving performance, such as biopharmaceutical purification, heterogeneous membrane reactors or functional nanoparticles remediation.

MATERIALS AND METHODS

Synthesis of the surfactant molecules. All chemicals used in this study were purchased from Sigma-Aldrich and used as received unless otherwise noted. Glycerol ($\geqslant$ 99.5%, Fisher Scientific, maximum water content 0.5%) was diluted with 10 wt.% deionized water (DI, R = 18 MΩ cm) to prepare 90 wt.% glycerol stock solution. Cross-linkers, including both pentaerythritol tetraacrylate (PETA) and hexanediol diacrylate (HDDA, Alfa Aesar) were doped with 1 wt.% photoinitiator 2-methoxy-2-phenylacetophenone (Acros Organics) before use. The cationic surfactants with variable alkyl chain lengths, 2-(acryloyloxy)ethyl dodecyl dimethyl ammonium bromide (AEDDAB, n5), 2-(acryloyloxy)ethyl tetradecyl dimethyl ammonium bromide (AETDAB, n6), 2-(acryloyloxy)ethyl hexadecyl dimethyl ammonium bromide (AEHDAB, n7) and 2-(acryloyloxy)ethyl octadecyl dimethyl ammonium bromide (AEODAB, n8) were synthesized through a modified one-step Menshukin reaction. Specifically, in a typical reaction, 1.00 mol 2-(dimethylamino)ethyl acrylate was mixed with 1.05 mol bromoalkanes (1-bromododecane, 1-bromotetradecane, 1-bromohexadecane, or 1-bromooctadecane) and 0.01 mol hydroquinone in a 500 mL round-bottom flask with a Teflon stir bar. The mixture was further diluted with 200 mL binary solvent composed of 50/50 (v/v) tetrahydrofuran and acetonitrile to form a homogeneous

solution and was stirred at 45°C for 48 hr. After 48 hr, the solution was allowed to cool to room temperature. Subsequently, the solid product was precipitated in excessive anhydrous diethyl ether 3 times, followed by drying *in vacuo* overnight.

Mesophase formulation and membrane casting. Mesophase thin-films with different limiting spacings were prepared in a fume hood operated in an air-conditioned environment with temperature regulated between 16 to 23°C and relative humidity varied between 10 to 40%. Namely, distinct ternary mixtures that self-assemble to H_I lyotropic mesophases were identified and cast in thin-films for further characterizations. n5t (composed by 76 wt.% AEDDAB, 4 wt.% PETA, and 20 wt.% glycerol), n6t (61 wt.% AETDAB, 4 wt.% PETA and 35 wt.% glycerol), n6d (61 wt.% AETDAB, 4 wt.% PETA and 35 wt.% glycerol), n7d (55 wt.% AEHDAB, 3 wt.% HDDA and 42 wt.% glycerol), and n8d (50 wt.% AEHDAB, 3 wt.% HDDA and 47 wt.% glycerol) were dissolved in ethyl acetate with predetermined concentrations. Subsequently, individual casting solutions were then filtered through a 0.2 μm polytetrafluoroethylene (PTFE) syringe filter (Fischer Brand) before use. In this manner, different H_I thin films with similar self-assembled structures but various domain spacings were fabricated through spin-coating the precursor solutions atop different substrates, including microscope glass slides, (100) silicon substrate, and silicon substrates covered with a thin layer of polyvinyl pyrrolidone (PVP) at a consistent spin-speed of 2000 rpm for 1 min, and let sit in ambient condition for extra 1 min. In order to prepare the PVP casting substrate, a 12 wt.% solution of 360 kg mol^{-1} PVP dissolved in ethanol was spin-coated atop pieces of the silicon substrate at 3000 rpm for 3 min. Subsequently, the silicon wafer with the PVP solution was transferred into a convection oven heated at 80°C for 30 min for complete solvent evaporation.

Nanofiltration membranes were fabricated as thin-film composites atop commercial ultrafiltration supports. Polyvinylidene fluoride ultrafiltration membranes (Synder V6 PVDF with MWCO 500 kg mol^{-1}) were purchased from the vendor. Membranes were rinsed in ethanol and spin-coated with a thin layer of the sacrificial thin film by 12 wt.% 360 kg mol^{-1} PVP from its ethanol solution, at 3000 rpm for 5 min. The 10wt.% mesophase solutions dissolved in ethyl acetate were subsequently cast atop the ultrafiltration supports using the same mesophase spin-coating protocol described above.

After the H_I mesophase thin-film casting, samples were immediately transferred into an enclosed nitrogen atmosphere. The photoinitiated cross-linking of films was conducted by illuminating a focused UV-beam (100-W Sunspot SM with 3 types of UV rays covering a range of wavelengths from ~275 to 450 nm) 8-cm above the substrate surface for 25 min. To examine the resiliency of H_I nanostructure in different solvent environments, some n6d silicon wafer supported thin-films were immersed in different organic solvents for 30 minutes, and were subsequently dried in high vacuum for further structural analysis.

Structural characterizations. The birefringence textures of the liquid crystal mesophases were analyzed using a Zeiss Axiovert 200M inverted microscope. A CCD camera photographed the corresponding micrographs for different mesophases before and after the photoinitiated cross-linking. Meanwhile, a JEOL 7500F Field-emission scanned electron microscope HR-SEM characterized the nanoscale morphology of the H_I membranes. For surface analysis, membranes were sectioned into 1 cm × 1 cm pieces using a razor blade. Vacuum-dried membranes were cryo-fractured in liquid nitrogen for cross-sectional imaging. Samples were mounted on standard stages and were sputter-coated with ~3 nm Iridium before loading into the microscope chamber.

Micrographs were captured at working distances from 6 to 8 mm with a constant accelerating voltage of 5 kV.

2D grazing-incidence small-angle X-ray scattering (GISAXS) data were collected by a Xeuss 2.0 from Xenocs at the Dual Source and Environmental X-ray Scattering facility operated by the Laboratory of Research on the Structure of Matter at the University of Pennsylvania. The scattering data were acquired from a GeniX3D Cu source (λ = 1.54 Å) at a constant sample to detector distance 55 cm covering accessible scattering vectors (q) 0.016 to 1.02 Å^{-1}. Samples were mounted on a GISAXS stage with the incident angle to the X-ray maintained from 0.15 to 0.25. After the scattering experiment, 1D integrated data were further processed by using the Foxtrot software package with the scattering intensity (I) versus $q = 4\pi sin(\theta)/\lambda$, where the scattering angle is 2θ. Silver behenate was the corresponding calibration standard. Since the perpendicular q projection q_z' is much greater than the critical angle q_c (~0.01 Å^{-1}), it was estimated that the $q_z \sim q_z'$ in the final 1-D plot.

Synthesis of CdSe nanoparticles. The synthesis of the oleic acid (OA) capped CdSe nanoparticles was performed following a previously reported hot-injection procedure (*55*). Specifically, CdO (0.79 mmol) was dissolved in a mixture of OA (3.9 mmol) and 1-octadecene (14 mL) in a 3-neck round bottom flask heated at 100°C to remove oxygen. The mixture was heated to 180°C until a homogeneous solution was acquired, followed by elevating the temperature to 250°C. At the same time, another solution was prepared by dissolving tri-n-octylphosphine (0.27 mmol) and Se (0.26 mmol) in 1-octadecene (2 mL). The CdSe nanoparticle was acquired by injecting the Se containing solution to the Cd containing solution at 250°C, and the mixture was allowed to cool down to room temperature after the injection. The product was then dissolved in toluene and precipitated in

methanol. The nanoparticles were then dispersed in hexane or isopropanol solution, and were used immediately in the following transport experiments after the synthesis. The nanoparticles were imaged using a JEOL F200 field emission transmission electron microscopy at an accelerating voltage of 200kV.

Transport experiments. The solvent permeation and solute rejection performance for different mesophase membranes was characterized using a dead-end 50-ml Amicon stirred cell (UFSC05001) equipped with a customized circular stainless-steel surface area reducer and a stir bar. The reducer exposes an active surface area of 2.4 cm^2 available for solvent permeation, and the cell was stirred at 400 rpm to reduce the concentration polarization during the rejection experiments. Membranes were placed in the stirred cells supported by the PP/PE nonwoven mat with their self-assembled layer facing the feed solution. Compressed nitrogen was provided by a dual-gauge regulator delivering transmembrane pressure up to 80 psi. After the membrane fabrication, the composite membranes were rinsed thoroughly with DI water for ~12 hr to detach the PVP layer sandwiched between the ultrafiltration support and the thin-film. The solvent permeance experiments (including DI water, methanol, ethanol, isopropanol, and hexane) were conducted in an air-conditioned environment with room temperature varied between 16 to 20 °C. The permeance of various solvents was generally measured following a sequence of DI water, hexane, methanol, ethanol, and isopropanol using transmembrane pressure from ~2 to 75 psi. Membranes were stored in DI water between each solvent permeance characterizations. In the case of the hexane permeation experiment, membranes were placed in an HP4750 stirred cell installed with a 25-mm membrane area reducer connected to a high-pressure hose supplying transmembrane

pressure at 400 psi. The permeated solvent was weighed every 5 minutes at different pressures to calculate the solvent permeance.

The single solute rejection experiment in aqueous solution was performed using 600 g mol^{-1} polyethylene glycol (with polydispersity index $Đ < 1.2$, Polymer Source, Inc) molecule dissolved in DI water with a concentration 1g L^{-1} as standard. The polymer solution was permeated through the membranes at a consistent flux ~12 L m^{-2} h^{-1}, and at least 5 ml permeate solution was collected during each rejection experiment. The polymer concentration at the permeate side was analyzed by a modified Dragendorff reagent method based on a Cary 100 ultraviolet-visible (UV-Vis) spectrophotometer that calculates the analyte abundance using Beer-Lambert's law. The molecular weight cut-off (MWCO) curves in methanol were determined by permeating dye molecules of different sizes with a concentration of 50 μM through the membrane at a consistent transmembrane pressure of 75 psi. Before each organic solvent rejection experiment, the membranes were first cleaned with saturated $NaNO_3$ methanol solution, followed by rinsing with excessive DI water and the pure organic solvent from the prospective rejection experiment.

Most solute rejection experiment in isopropanol was determined by permeating the single solute solution containing 50 μM dye molecules, 5 μM CdSe, or mixtures of dyes and CdSe at the concentrations as mentioned above through the membranes with a consistent flux ~10 L m^{-2} h^{-1}. In the solute competitive solute rejection experiment with the acid fuchsin, a higher CdSe concentration 50 μM was involved. During the organic solvent nanofiltration experiment, the sample collection was started once a steady-state permeate concentration was observed, and at least 5 ml permeate solution was collected for further analysis using the UV-Vis spectrophotometer. In the mixture solvent permeation using a consistent transmembrane pressure drop at 75 psi, an equal volume of isopropanol and hexane prepared 50 μM CdSe feed solution. The retentate

solution and the concentrated solution (concentration normalized to retentate) containing equal volume hexane and isopropanol were further analyzed by an Edinburgh Instruments FLS 1000 fluorescence spectrometer that excited the samples using a 365 nm monochromated Xe arc lamp.

SUPPLEMENTARY MATERIALS

Supplementary material for this article is available at http://advances.sciencemag.org

REFERENCES AND NOTES

1. R. P. Lively, D. S. Sholl, From water to organics in membrane separations. *Nat. Mater.* **16**, 276-279 (2017).
2. D. S. Sholl, R. P. Lively, Seven chemical separations to change the world. *Nature* **532**, 435-437 (2016).
3. K. A. Thompson, R. Mathias, D. Kim, J. Kim, N. Rangnekar, J. Johnson, S. J. Hoy, I. Bechis, A. Tarzia, K. E. Jelfs, N-Aryl–linked spirocyclic polymers for membrane separations of complex hydrocarbon mixtures. *Science* **369**, 310-315 (2020).
4. P. Marchetti, M. F. Jimenez Solomon, G. Szekely, A. G. Livingston, Molecular separation with organic solvent nanofiltration: a critical review. *Chem. Rev.* **114**, 10735-10806 (2014).
5. C. Liu, G. Dong, T. Tsuru, H. Matsuyama, Organic solvent reverse osmosis membranes for organic liquid mixture separation: A review. *J. Membr. Sci.* **620**, 118882 (2021).
6. M. Galizia, K. P. Bye, Advances in organic solvent nanofiltration rely on physical chemistry and polymer chemistry. *Front. Chem.* **6**, 511 (2018).
7. S. Hermans, H. Mariën, C. Van Goethem, I. F. Vankelecom, Recent developments in thin film (nano)composite membranes for solvent resistant nanofiltration. *Curr. Opin. Chem. Eng.* **8**, 45-54 (2015).
8. H. B. Park, J. Kamcev, L. M. Robeson, M. Elimelech, B. D. Freeman, Maximizing the right stuff: The trade-off between membrane permeability and selectivity. *Science* **356**, 1137 (2017).
9. D. L. Gin, R. D. Noble, Designing the next generation of chemical separation membranes. *Science* **332**, 674-676 (2011).
10. V. Freger, Nanoscale heterogeneity of polyamide membranes formed by interfacial polymerization. *Langmuir* **19**, 4791-4797 (2003).
11. A. W. Mohammad, Y. H. Teow, W. L. Ang, Y. T. Chung, D. L. Oatley-Radcliffe, N. Hilal, Nanofiltration membranes review: Recent advances and future prospects. *Desalination* **356**, 226-254 (2015).
12. J. Luo, Y. Wan, Effects of pH and salt on nanofiltration—a critical review. *J. Membr. Sci.* **438**, 18-28 (2013).
13. S. Karan, Z. Jiang, A. G. Livingston, Sub–10 nm polyamide nanofilms with ultrafast solvent transport for molecular separation. *Science* **348**, 1347-1351 (2015).
14. P. Gorgojo, S. Karan, H. C. Wong, M. F. Jimenez-Solomon, J. T. Cabral, A. G. Livingston, Ultrathin polymer films with intrinsic microporosity: anomalous solvent permeation and high flux membranes. *Adv. Funct. Mater.* **24**, 4729-4737 (2014).
15. M. F. Jimenez-Solomon, Q. Song, K. E. Jelfs, M. Munoz-Ibanez, A. G. Livingston, Polymer nanofilms with enhanced microporosity by interfacial polymerization. *Nat. Mater.* **15**, 760-767 (2016).
16. B. Liang, H. Wang, X. Shi, B. Shen, X. He, Z. A. Ghazi, N. A. Khan, H. Sin, A. M. Khattak, L. Li, Microporous membranes comprising conjugated polymers with rigid backbones enable ultrafast organic-solvent nanofiltration. *Nat. Chem.* **10**, 961-967 (2018).
17. S. Kandambeth, B. P. Biswal, H. D. Chaudhari, K. C. Rout, S. Kunjattu H, S. Mitra, S. Karak, A. Das, R. Mukherjee, U. K. Kharul, B. Rahul, Selective molecular sieving in self-standing porous covalent-organic-framework membranes. *Adv. Mater.* **29**, 1603945 (2017).

18. D. B. Shinde, G. Sheng, X. Li, M. Ostwal, A.-H. Emwas, K.-W. Huang, Z. Lai, Crystalline 2D covalent organic framework membranes for high-flux organic solvent nanofiltration. *J. Am. Chem. Soc.* **140**, 14342-14349 (2018).
19. E. Barankova, X. Tan, L. F. Villalobos, E. Litwiller, K. V. Peinemann, A metal chelating porous polymeric support: the missing link for a defect-free metal–organic framework composite membrane. *Angew. Chem., Int. Ed.* **56**, 2965-2968 (2017).
20. J. R. Werber, C. O. Osuji, M. Elimelech, Materials for next-generation desalination and water purification membranes. *Nat. Rev. Mater.* **1**, 16018 (2016).
21. D. L. Gin, X. Lu, P. R. Nemade, C. S. Pecinovsky, Y. Xu, M. Zhou, Recent advances in the design of polymerizable lyotropic liquid-crystal assemblies for heterogeneous catalysis and selective separations. *Adv. Funct. Mater.* **16**, 865-878 (2006).
22. T. Kato, J. Uchida, T. Ichikawa, T. Sakamoto, Functional liquid crystals towards the next generation of materials. *Angew. Chem., Int. Ed.* **57**, 4355-4371 (2018).
23. X. Feng, M. E. Tousley, M. G. Cowan, B. R. Wiesenauer, S. Nejati, Y. Choo, R. D. Noble, M. Elimelech, D. L. Gin, C. O. Osuji, Scalable fabrication of polymer membranes with vertically aligned 1 nm pores by magnetic field directed self-assembly. *ACS Nano* **8**, 11977-11986 (2014).
24. T. Ichikawa, T. Kato, H. Ohno, 3D continuous water nanosheet as a gyroid minimal surface formed by bicontinuous cubic liquid-crystalline zwitterions. *J. Am. Chem. Soc.* **134**, 11354-11357 (2012).
25. T. Sakamoto, T. Ogawa, H. Nada, K. Nakatsuji, M. Mitani, B. Soberats, K. Kawata, M. Yoshio, H. Tomioka, T. Sasaki, M. Kimura, M. Henmi, T. Kato, Development of nanostructured water treatment membranes based on thermotropic liquid crystals: molecular design of sub-nanoporous materials. *Adv. Sci.* **5**, 1700405 (2018).
26. X. Feng, S. Nejati, M. G. Cowan, M. E. Tousley, B. R. Wiesenauer, R. D. Noble, M. Elimelech, D. L. Gin, C. O. Osuji, Thin polymer films with continuous vertically aligned 1 nm pores fabricated by soft confinement. *ACS Nano* **10**, 150-158 (2016).
27. O. Q. Imran, N. K. Kim, L. N. Bodkin, G. E. Dwulet, X. Feng, K. Kawabata, M. Elimelech, D. L. Gin, C. O. Osuji, Nanoscale thickness control of nanoporous films derived from directionally photopolymerized mesophases. *Adv. Mater. Interfaces* **8**, 2001977 (2021).
28. S. M. Dischinger, J. Rosenblum, R. D. Noble, D. L. Gin, Evaluation of a nanoporous lyotropic liquid crystal polymer membrane for the treatment of hydraulic fracturing produced water via cross-flow filtration. *J. Membr. Sci.* **592**, 117313 (2019).
29. J. E. Bara, A. K. Kaminski, R. D. Noble, D. L. Gin, Influence of nanostructure on light gas separations in cross-linked lyotropic liquid crystal membranes. *J. Membr. Sci.* **288**, 13-19 (2007).
30. M. Zhou, P. R. Nemade, X. Lu, X. Zeng, E. S. Hatakeyama, R. D. Noble, D. L. Gin, New type of membrane material for water desalination based on a cross-linked bicontinuous cubic lyotropic liquid crystal assembly. *J. Am. Chem. Soc.* **129**, 9574-9575 (2007).
31. B. M. Carter, B. R. Wiesenauer, E. S. Hatakeyama, J. L. Barton, R. D. Noble, D. L. Gin, Glycerol-based bicontinuous cubic lyotropic liquid crystal monomer system for the fabrication of thin-film membranes with uniform nanopores. *Chem. Mater.* **24**, 4005-4007 (2012).
32. C. R. Kasprzak, E. T. Scherzinger, A. Sarkar, M. Miao, D. H. Porcincula, A. M. Madriz, Z. M. Pennewell, S. S. Chau, R. Fernando, M. Stefik, S. Zhang, Ordered nanostructures of

carbon nanotube–polymer composites from lyotropic liquid crystal templating. *Macromol. Chem. Phys.* **219**, 1800197 (2018).
33. M. A. DePierro, C. A. Guymon, Polymer structure development in lyotropic liquid crystalline solutions. *Macromolecules* **47**, 5728-5738 (2014).
34. G. P. Sorenson, K. L. Coppage, M. K. Mahanthappa, Unusually stable aqueous lyotropic gyroid phases from gemini dicarboxylate surfactants. *J. Am. Chem. Soc.* **133**, 14928-14931 (2011).
35. X. Feng, K. Kawabata, G. Kaufman, M. Elimelech, C. O. Osuji, Highly selective vertically aligned nanopores in sustainably derived polymer membranes by molecular templating. *ACS Nano* **11**, 3911-3921 (2017).
36. M. E. Tousley, X. Feng, M. Elimelech, C. O. Osuji, Aligned nanostructured polymers by magnetic-field-directed self-assembly of a polymerizable lyotropic mesophase. *ACS Appl. Mater. Interfaces* **6**, 19710-19717 (2014).
37. X. Feng, K. Kawabata, M. G. Cowan, G. E. Dwulet, K. Toth, L. Sixdenier, A. Haji-Akbari, R. D. Noble, M. Elimelech, D. L. Gin, Single crystal texture by directed molecular self-assembly along dual axes. *Nat. Mater.* **18**, 1235-1243 (2019).
38. X. Feng, Q. Imran, Y. Zhang, L. Sixdenier, X. Lu, G. Kaufman, U. Gabinet, K. Kawabata, M. Elimelech, C. O. Osuji, Precise nanofiltration in a fouling-resistant self-assembled membrane with water-continuous transport pathways. *Sci. Adv.* **5**, eaav9308 (2019).
39. Y. Zhang, R. Dong, U. R. Gabinet, R. Poling-Skutvik, N. K. Kim, C. Lee, O. Q. Imran, X. Feng, C. O. Osuji, Rapid fabrication by lyotropic self-assembly of thin nanofiltration membranes with uniform 1 nanometer pores. *ACS Nano* **15**, 8192-8203 (2021).
40. W. A. Phillip, M. A. Hillmyer, E. L. Cussler, Cylinder orientation mechanism in block copolymer thin films upon solvent evaporation. *Macromolecules* **43**, 7763-7770 (2010).
41. C. Sinturel, M. Vayer, M. Morris, M. A. Hillmyer, Solvent vapor annealing of block polymer thin films. *Macromolecules* **46**, 5399-5415 (2013).
42. A. Faraone, S. Magazu, G. Maisano, P. Migliardo, E. Tettamanti, V. Villari, The puzzle of poly (ethylene oxide) aggregation in water: Experimental findings. *J. Chem. Phys.* **110**, 1801-1806 (1999).
43. M. Meireles, A. Bessieres, I. Rogissart, P. Aimar, V. Sanchez, An appropriate molecular size parameter for porous membranes calibration. *J. Membr. Sci.* **103**, 105-115 (1995).
44. J. Shao, R. E. Baltus, Hindered diffusion of dextran and polyethylene glycol in porous membranes. *AIChE J.* **46**, 1149-1156 (2000).
45. M. Sobera, C. Kleijn, Hydraulic permeability of ordered and disordered single-layer arrays of cylinders. *Phys. Rev. E* **74**, 036301 (2006).
46. J. Drummond, M. Tahir, Laminar viscous flow through regular arrays of parallel solid cylinders. *Int. J. Multiphase Flow* **10**, 515-540 (1984).
47. L. J. Zeman, A. Zydney, *Microfiltration and Ultrafiltration: Principles and Applications* (Marcel Dekker, New York, 1996).
48. A. Buekenhoudt, F. Bisignano, G. De Luca, P. Vandezande, M. Wouters, K. Verhulst, Unravelling the solvent flux behaviour of ceramic nanofiltration and ultrafiltration membranes. *J. Membr. Sci.* **439**, 36-47 (2013).
49. S. Sorribas, P. Gorgojo, C. Téllez, J. Coronas, A. G. Livingston, High flux thin film nanocomposite membranes based on metal–organic frameworks for organic solvent nanofiltration. *J. Am. Chem. Soc.* **135**, 15201-15208 (2013).

50. L. F. Villalobos, T. Huang, K. V. Peinemann, Cyclodextrin films with fast solvent transport and shape-selective permeability. *Adv. Mater.* **29**, 1606641 (2017).
51. J. Liu, D. Hua, Y. Zhang, S. Japip, T. S. Chung, Precise molecular sieving architectures with Janus pathways for both polar and nonpolar molecules. *Adv. Mater.* **30**, 1705933 (2018).
52. T. Huang, T. Puspasari, S. P. Nunes, K. V. Peinemann, Ultrathin 2D-layered cyclodextrin membranes for high-performance organic solvent nanofiltration. *Adv. Funct. Mater.* **30**, 1906797 (2020).
53. T. Huang, B. A. Moosa, P. Hoang, J. Liu, S. Chisca, G. Zhang, M. AlYami, N. M. Khashab, S. P. Nunes, Molecularly-porous ultrathin membranes for highly selective organic solvent nanofiltration. *Nat. Commun.* **11**, 5822 (2020).
54. B. Guzelturk, O. Erdem, M. Olutas, Y. Kelestemur, H. V. Demir, Stacking in colloidal nanoplatelets: tuning excitonic properties. *ACS Nano* **8**, 12524-12533 (2014).
55. J. Chen, J. Song, X. Sun, W. Deng, C. Jiang, W. Lei, J. Huang, R. Liu, An oleic acid-capped CdSe quantum-dot sensitized solar cell. *Appl. Phys. Lett.* **94**, 153115 (2009).
56. Y.-x. Shen, W. Song, D. R. Barden, T. Ren, C. Lang, H. Feroz, C. B. Henderson, P. O. Saboe, D. Tsai, H. Yan, Achieving high permeability and enhanced selectivity for Angstrom-scale separations using artificial water channel membranes. *Nat. Commun.* **9**, 2294 (2018).
57. B. Van der Bruggen, J. Schaep, D. Wilms, C. Vandecasteele, Influence of molecular size, polarity and charge on the retention of organic molecules by nanofiltration. *J. Membr. Sci.* **156**, 29-41 (1999).

Acknowledgments

Funding: Portions of this work were made possible with support from N.S.F. through PFI:AIR-TT IIP-1640375 and CBET1703494. Facilities use was supported by the Singh Center for Nanotechnology at the University of Pennsylvania, and the Dual Source and Environmental X-ray scattering facility operated by the Laboratory for Research on the Structure of Matter at the University of Pennsylvania (NSF MRSEC 17-20530). The equipment purchase was made possible by NSF MRI grant (17-25969), ARO DURIP grant (W911NF-17-1-0282), and the University of Pennsylvania. C.O.O. also acknowledges additional financial support from N.S.F. (DMR-1945966). Y.Z. acknowledges financial support from Shanghai University.

Author contributions: Y.Z., X.F. and C.O.O. conceived the ideas and designed the study. Y.Z. performed the materials synthesis, structural characterizations, membrane fabrication and transport experiments. R.D. performed structural characterization experiments. D.K. synthesized the photoluminescent nanoparticles. All authors contributed to data analysis. Y.Z. and C.O.O. contributed the manuscript writing.

Competing interests: The authors declare no competing financial interest.

Data and materials availability: All data needed to evaluate the conclusions in the paper are present in the paper and/or the Supplementary Materials. Additional data related to this paper may be requested from the authors.